ATLAS PUB Note
ATL-PHYS-PUB-2023-012
25th May 2023

Effective field theory interpretation of the measurement of off-shell Higgs boson production from $ZZ \rightarrow 4\ell$ and $ZZ \rightarrow 2\ell2\nu$ decay channels with the ATLAS detector

The ATLAS Collaboration

This note reports on the effective field theory (EFT) interpretation of the measurement of off-shell Higgs boson production using 139 fb^{-1} of proton-proton collision data at a centre-of-mass energy of 13 TeV, collected by the ATLAS detector at the Large Hadron Collider. Higgs boson decays to $ZZ \rightarrow 4\ell$ and $ZZ \rightarrow 2\ell2\nu$ final states, with $\ell = e$ or μ, are considered. Off-shell Higgs boson events with masses of the order of 1 TeV are sensitive to phenomena beyond the Standard Model. Furthermore, the Higgs boson coupling to the top quark and its effective coupling to the gluon are degenerate in the inclusive on-shell measurements while the off-shell events can break the degeneracy. EFT operators affecting these couplings are studied and their associated Wilson coefficients are observed (expected) to be [-9, 18] ([-9, 17]) for $c_{t\varphi}$ (Higgs-top coupling modifier) and [-0.04, 0.03] ([-0.04, 0.03]) for $c_{\varphi G}$ (Higgs-gluon coupling modifier) at the 95% confidence level with new physics energy scale $\Lambda = 1$ TeV, in agreement with the SM prediction.

1 Introduction

Detecting possible contributions from new processes beyond the Standard Model (SM) is crucial for understanding phenomena such as dark matter or the dominance of the universe by matter for which the SM provides no explanation. The Higgs boson, the physical state associated with the mechanism responsible for the origin of mass for other particles in the SM, provides a pivotal window for searching for possible beyond the Standard Model (BSM) physics. This note reports on a search for BSM physics using off-shell Higgs boson events in the 4ℓ and $2\ell 2\nu$ final states, in the region $m_{ZZ} > 220\,\text{GeV}$ where m_{ZZ} is the invariant mass of two Z bosons. The search is carried out by re-interpreting a previously reported measurement of off-shell Higgs boson production [1].

Off-shell Higgs boson production is accessible only in the ZZ or WW final states at the LHC, where the increase in available phase space for the Higgs decay as m_H approaches twice the gauge Z boson mass cancels out the rapid fall-off in production moving away from the Higgs on-shell peak. In the ZZ final state, off-shell Higgs boson production accounts for only $O(10\%)$ of the total Higgs cross-section [2]. As a result, most BSM constraints are obtained from studies in the on-shell region. However, off-shell Higgs boson events offer the opportunity to probe a higher energy scale, where BSM physics may emerge. Furthermore, the ATLAS and CMS experiments [3]) have shown that the Higgs-top and effective Higgs-gluon couplings in the gluon-gluon fusion (ggF) Higgs production mode cannot be measured independently using inclusive measurements in the on-shell region, while the off-shell Higgs boson offers a means to decouple them [4]. Some other study [5] shows that the Higgs-top coupling can be probed directly in the $t\bar{t}H$ channel. This note will only focus on the ggF production mode based on the Effective Field Theory (EFT) framework to search for BSM physics, with the full ATLAS Run-2 pp collision dataset. Section 2 discusses the EFT formalism used to perform the analysis, and Section 3 how the BSM couplings being probed were modelled. Section 4 describes the ATLAS detector and Section 5 the data and Monte Carlo (MC) simulation samples used, while Section 6 covers the analysis in both final states. Section 7 presents the systematic uncertainties taken into account, and the final results are shown in Section 8.

2 Theoretical frameworks and motivation

The results presented in this note are provided in the context of two frameworks commonly used for studying the off-shell Higgs boson in the ZZ decay channel: a simplified effective coupling approach which we refer to as the $c_g - c_t$ framework [4] (or the similar κ-framework [6]) and the full Warsaw basis of the Standard Model Effective Field Theory (SMEFT) framework [7]. The former framework offers a more direct connection to physics, while the latter allows for a common interpretation of Higgs, electroweak, and top physics measurements.

2.1 $c_g - c_t$ framework

The Lagrangian presented in Ref. [4] is considered, which includes three dimension-six operators that contribute to the gluon-gluon fusion process (ggF):

$$\mathcal{L}^{\text{dim-6}} = c_y \frac{y_t|\varphi|^2}{v^2}\bar{Q}_L\tilde{\varphi}t_R + \text{h.c.} + \frac{c_g g_s^2}{48\pi^2 v^2}|\varphi|^2 G_{\mu\nu}G^{\mu\nu} + \tilde{c}_g \frac{g_s^2}{32\pi^2 v^2}|\varphi|^2 G_{\mu\nu}\tilde{G}^{\mu\nu} \tag{1}$$

The notation from the paper was adapted for consistency with the other model in Section 2.2. After spontaneous symmetry breaking, the full SMEFT Lagrangian, which includes the SM and dimension-six contributions, is

$$\begin{aligned}\mathcal{L}_{\mathrm{SMEFT}} &\supset \mathcal{L}_{\mathrm{SM}} + \mathcal{L}^{\text{dim-6}} \\ &= - c_t \frac{m_t}{v}\bar{t}tH + c_g \frac{g_s^2 H}{48\pi^2 v} G_{\mu\nu}G^{\mu\nu} \qquad (\mathrm{CP-even}) \\ &\quad + i\tilde{c}_t \frac{m_t}{v}\bar{t}\gamma_5 tH + \tilde{c}_g \frac{g_s^2 H}{32\pi^2 v} G_{\mu\nu}\tilde{G}^{\mu\nu} \quad (\mathrm{CP-odd})\end{aligned} \tag{2}$$

where $c_t = 1 - \mathrm{Re}(\mathrm{c}_y)$ and $\tilde{c}_t = \mathrm{Im}(c_y)$. Only CP-even operators are considered in this analysis as the observables used in this analysis were not designed to be CP-sensitive. The Feynman diagrams related to the Higgs-top coupling c_t and Higgs-gluon coupling c_g are shown in Figure 1. In the SM, $c_g = 0$ and $c_t = 1$.

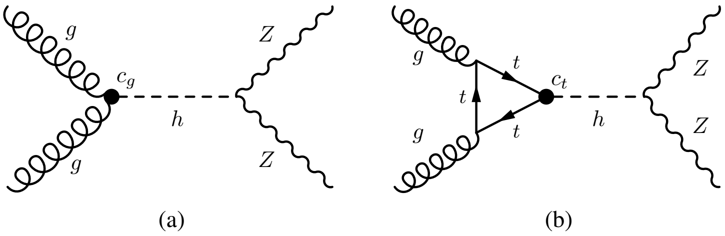

(a) (b)

Figure 1: The representative leading-order diagrams in the $gg \to ZZ$ channel, showing where the 1(a) Higgs-gluon effective coupling and 1(b) Higgs-top coupling are modified by the corresponding operators in the $c_t - c_g$ framework.

The inclusive ggF cross-section in this framework can be calculated and normalized to the SM prediction to yield [6]:

$$\frac{\sigma^{\mathrm{SMEFT}}(c_t, c_g)}{\sigma^{\mathrm{SM}}} \simeq (c_t + c_g)^2 \left(1 - \frac{7}{15}\frac{c_g}{c_t + c_g}\frac{m_H^2}{4m_t^2}\right) \tag{3}$$

In the on-shell Higgs boson region, the mass-dependent term can be neglected, yielding

$$\frac{\sigma^{\mathrm{SMEFT}}_{\mathrm{on-shell}}(c_t, c_g)}{\sigma^{\mathrm{SM}}_{\text{on-shell}}} \simeq (c_t + c_g)^2 \tag{4}$$

This is the source of the coupling degeneracy: as the SMEFT on-shell signal strength is only dependent on the sum of c_t and c_g, they cannot be measured separately in the on-shell regime. However, for the off-shell Higgs production, for which $m_{ZZ} > m_t$, the mass term in Equation 3 can no longer be ignored. Therefore, measurements using off-shell events can probe c_t and c_g separately.

2.2 Warsaw basis

Another widely used framework for the EFT interpretation of the Higgs measurements is based on the Warsaw basis. In this framework, the Lagrangian of the SMEFT is expanded with respect to an energy scale Λ:

$$\mathcal{L}_{\mathrm{SMEFT}} = \mathcal{L}_{\mathrm{SM}} + \sum_{\forall i, \forall d>4} \frac{C_i^{(d)}}{\Lambda^{d-4}} O_i^{(d)} \tag{5}$$

Here, Λ is the scale at which new physics is expected to appear and d refers to the dimensionality of the operators in the effective Lagrangian. It can be associated with a possible UV-complete BSM model that contributes to the EFT operators. Similarly, $C_i^{(d)}$ are the Wilson coefficients that encode information about the couplings associated with the possible UV-complete model.

In this analysis, only dimension-six operators are considered. Dimension-five operators are neglected due to the current neutrino mass bounds and lepton- and baryon-number conservation assumptions in this analysis. Dimension-seven operators are suppressed by another factor of the new physics scale compared with dimension-six operators. Among many dimension-six operators, only Higgs-gluon and Higgs-top related operators in the $gg \to ZZ$ channel are considered, as discussed in Section 2.1. The corresponding definitions are summarized in Table 1 and the leading-order Feynman diagrams are depicted in Figure 2. In the SM, $c_{\varphi G} = 0$ and $c_{t\varphi} = 0$.

Operator	Coefficient (Λ^{-2})	Definition
$O_{\varphi G}$	$c_{\varphi G}$	$(\varphi^\dagger \varphi - \frac{v^2}{2}) G_A^{\mu\nu} G_{\mu\nu}^A$
$O_{t\varphi}$	$c_{t\varphi}$	$(\varphi^\dagger \varphi - \frac{v^2}{2}) \bar{Q}_L \tilde{\varphi} t_R$ + h.c.

Table 1: Operators of interest in the Warsaw basis and their definitions. See more details in [8].

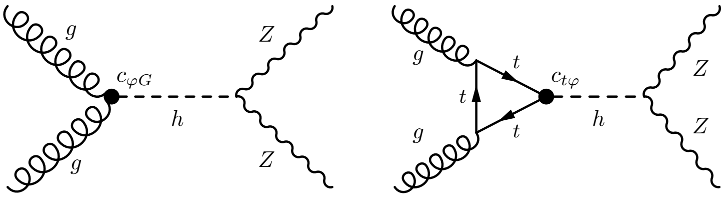

(a) (b)

Figure 2: The representative leading-order diagrams in the $gg \to ZZ$ channel, showing where (a) the effective Higgs-gluon coupling and (b) the top-Higgs coupling are modified by the corresponding Warsaw basis operators.

The analysis reported in this note is performed in the SMEFT framework using the Warsaw basis. Nevertheless, by comparing Equation 2 and Table 1 (Equation 2 includes contributions from both the SM and BSM while Table 1 is pure BSM), translation between the two frameworks can be accomplished by

$$\begin{aligned} c_{t\varphi} &= -\frac{y_t \Lambda^2}{v^2}(c_t - 1) \\ c_{\varphi G} &= \frac{g_s^2 \Lambda^2}{48\pi^2 v^2} c_g \end{aligned} \tag{6}$$

and results can therefore be recast in the $c_g - c_t$ framework accordingly.

3 Modelling of BSM couplings

The total cross-section corresponding to the Lagrangian in Equation 5 can be expressed as:

$$\sigma^{\text{SMEFT}} \propto |\mathcal{M}_{\text{SMEFT}}|^2 = |\mathcal{M}_{\text{SM}}|^2 + 2\sum_{\forall i} \frac{C_i^{(6)}}{\Lambda^2} \text{Re}\left(\mathcal{M}_{\text{SM}}^* \cdot \mathcal{M}_i^{(6)}\right) + \sum_{\forall i,j} \frac{C_i^{(6)} C_j^{(6)}}{\Lambda^4} \text{Re}\left(\mathcal{M}_i^{*(6)} \cdot \mathcal{M}_j^{(6)}\right) \tag{7}$$

or simply

$$\sigma^{\text{SMEFT}} = \sigma^{\text{SM}} + \sigma^{\text{int}} + \sigma^{\text{BSM}} \tag{8}$$

The first term on the right-hand side of both equations 7 and 8 corresponds to the SM contribution only. The second term represents the interference between the SM and BSM (referred to as the EFT dimension-d linear term with $d = 6$, or the EFT linear term for short). The third term is the pure contribution from BSM (referred to as the EFT dimension-d quadratic term with $d = 6$, or the EFT quadratic term for short), while the last term is called the cross-term (also pure BSM contributions).

To measure the potential BSM couplings listed in Table 1, Equation 8 can be explicitly rewritten as follows:

$$\begin{aligned} \sigma^{\text{SMEFT}} = \sigma^{\text{SM}} &+ c_{\varphi G}\, \sigma^{O_{\varphi G}\text{SM}} + c_{\varphi G}^2\, \sigma^{O_{\varphi G}\text{Squared}} \\ &+ c_{t\varphi}\, \sigma^{O_{t\varphi}\text{SM}} + c_{t\varphi}^2\, \sigma^{O_{t\varphi}\text{Squared}} \\ &+ c_{\varphi G}\, c_{t\varphi}\, \sigma^{O_{\varphi G} O_{t\varphi}} \end{aligned} \tag{9}$$

where

- $\sigma^{O_{\varphi G}\text{SM}}$ ($\sigma^{O_{t\varphi}\text{SM}}$) is the interference term of the EFT dimension-six operator $O_{\varphi G}$ ($O_{t\varphi}$) with the SM.
- $\sigma^{O_{\varphi G}\text{Squared}}$ ($\sigma^{O_{t\varphi}\text{Squared}}$) is the quadratic term of $O_{\varphi G}$ ($O_{t\varphi}$).
- $\sigma^{O_{\varphi G} O_{t\varphi}}$ is the cross-term of $O_{\varphi G}$ and $O_{t\varphi}$, corresponding to matrix element $2 \cdot \text{Re}\left(\mathcal{M}_{O_{\varphi G}}^* \cdot \mathcal{M}_{O_{t\varphi}}\right)$.

The EFT operator-related cross-sections on the right-hand side of the equation 9 are obtained by setting the corresponding coefficients to be 1. For example, in the above equation, $\sigma^{O_{\varphi G}\text{SM}}$ refers to $\sigma^{O_{\varphi G}\text{SM}}(c_{\varphi G} = 1)$, $\sigma^{O_{\varphi G}\text{Squared}} = \sigma^{O_{\varphi G}\text{Squared}}(c_{\varphi G} = 1)$, $\sigma^{O_{\varphi G} O_{t\varphi}} = \sigma^{O_{\varphi G} O_{t\varphi}}(c_{\varphi G} = 1 \text{ and } c_{t\varphi} = 1)$.

Two fit configurations are considered for SMEFT results: the *linear-only fit* which includes terms of order up to $\Lambda^{-2}$and the *linear+quadratic fit* extending up to Λ^{-4}. For the 2-dimensional (dimension here refers to the number of coefficients) $c_{\varphi G}$-$c_{t\varphi}$ fits, $\sigma^{O_{\varphi G}\text{Squared}}$, $\sigma^{O_{t\varphi}\text{Squared}}$ and $\sigma^{O_{\varphi G} O_{t\varphi}}$ are not incorporated in the linear-only fit but are considered in the linear+quadratic fit because each cross-section of them is $\propto \Lambda^{-4}$.

The parameterization of the predicted cross-section is computed as a relative correction to the SM prediction computed at the highest available order:

$$\sigma^{\mathrm{SMEFT}} = \sigma^{\mathrm{SM}}_{\mathrm{N^3LO}} \times (1 + \frac{\sigma^{\mathrm{int}}_{\mathrm{LO}}}{\sigma^{\mathrm{SM}}_{\mathrm{LO}}} + \frac{\sigma^{\mathrm{BSM}}_{\mathrm{LO}}}{\sigma^{\mathrm{SM}}_{\mathrm{LO}}}) \tag{10}$$

The effect of dimension-six operators can have an important correction on the total width of the intermediate particles in cases where the intermediate particles are on-shell. However, it is pointed out that the cross-section of the off-shell Higgs is independent of the total Higgs decay width [9]. Therefore, the impact of the dimension-six operators on the total Higgs width can be neglected.

The difference between the original measurement reported in Ref. [1] and this EFT analysis lies in the parameter to interpret. In the original measurement, the EFT operators are not considered and the analysis fits the off-shell Higgs signal strength $\mu_{\text{off-shell}}$, where $\mu_{\text{off-shell}} = \sigma^{\text{observed data}}/\sigma^{\mathrm{SM}}$. However, in the EFT interpretation, EFT operators in Equation 9 are included in the parametrization and dimension-six coefficients are fit, while the signal strengths are set to the SM prediction, i.e., $\mu_{\text{off-shell}} = \mu^{\mathrm{ggF}}_{\text{off-shell}} = \mu^{\mathrm{EW}}_{\text{off-shell}} = 1$. Or equivalently, the $\mu_{\text{off-shell}}$ in the original measurement is expressed in terms of the SMEFT dimension-six parameters in the EFT analysis.

4 ATLAS detector

The ATLAS detector is described in detail in [10]. As a multipurpose detector, ATLAS has a symmetric cylindrical geometry in the forward-backward direction and covers a near 4π solid angle [1]. It consists of an inner tracking detector, electromagnetic and hadron calorimeters, a muon spectrometer, and a trigger system. The inner tracking detector (ID) is immersed in a 2T magnetic field provided by a thin superconducting solenoid surrounded. There are three main components in the ID: a silicon pixel detector, a semiconductor tracker, and a transition radiation tracker, with a total coverage of the pseudorapidity range $|\eta| < 2.5$. Lead/liquid-argon (LAr) sampling calorimeters measure the electromagnetic (EM) energy of particles with high granularity covering the region $|\eta| < 3.2$, while the steel/scintillator-tile hadron calorimeter covers the central pseudorapidity range $|\eta| < 1.7$. The endcap and forward regions $1.5 < |\eta| < 4.9$ are covered by the LAr calorimeters to measure both the electromagnetic and hadronic energy. The muon spectrometer surrounding the calorimeters is incorporating large superconducting toroidal air-core magnets. The muon tracking is provided by three layers of precision wire chambers in the range of $|\eta| < 2.7$ and dedicated fast chambers are used to trigger the events in the region $|\eta| < 2.4$. The whole trigger system has two levels to select events of interest. The first level is implemented in hardware and uses the detector information to reduce the rate of events accepted below 100 kHz. This is further decreased by the second level, a software-based trigger or the high-level trigger, down to 1k events per second on average. An extensive and dedicated software suite [11] is used to simulate data, reconstruct and analyze observed and simulated data, operate detectors, and trigger and acquire data of the experiment.

---

[1] A right-handed coordinate system is used at ATLAS with the origin at the nominal interaction point (IP) at the centre of the detector. The z-axis is along the beam pipe. The x-axis points to the centre of the LHC ring from the IP, and the y-axis points upwards. n the transverse plane, the cylindrical coordinates (r, ϕ) are used with ϕ being the azimuthal angle from the z-axis. The pseudorapidity is defined as $\eta = -\ln\tan(\theta/2)$ where θ is the polar angle. Angular distance is measured as $\Delta R \equiv \sqrt{(\Delta\eta)^2 + (\Delta\phi)^2}$.

5 Data and Monte Carlo simulation

5.1 Data

The proton-proton (pp) collision data used in this analysis was collected in the years 2015 to 2018 at the ATLAS detector, corresponding to an integrated luminosity of 139 fb^{-1}. The overall trigger efficiency for the off-shell signal process is larger than 98%.

5.2 Simulation of BSM processes

MC samples for dimension-six operators are simulated at next to leading order (NLO) accuracy in QCD by MadGraph5_aMC@NLOv2.7.3 [12] using the model SMEFT@NLO UFO[8] based on the Warsaw basis and the NNPDF3.0 NNLO PDF set [13]. The interference terms of tree-level and loop-induced diagrams are generated using a reweighting scheme [14]. Input parameters adopt the G_F, m_Z, m_W scheme: their values and the values of the new physics energy scale Λ and EFT renormalization scale μ_{EFT} are given in Table 2. Gauge unitary and Cabibbo–Kobayashi–Maskawa (CKM) matrix unitarity are required. Events are interfaced to Pythiav8.244 [15], with the A14 tune [16] for parton showering and hadronization. A matching procedure is performed to remove phase-space overlap between the jets from the matrix element and those from showers, using the MLM algorithm [17]. The linear, quadratic, and cross-term samples, mentioned in Equation 9, are generated separately. No operators with mass dimension higher than six are considered.

Parameter	Symbol	Value
New physics energy scale	Λ	1 TeV
EFT renormalization scale	μ_{EFT}	175 GeV ($\approx m_t$)
Fermi constant	G_F	1.1663787×10^{-5} GeV^{-2}
Z boson mass	m_Z	91.18760 GeV
W boson mass	m_W	79.8244 GeV

Table 2: Values of parameters used in MC event simulations of EFT dimension-six operators.

5.3 Simulation of SM processes

The MC simulation of SM processes is discussed in detail in Ref. [1]. Briefly, the SM loop-induced processes $gg \to ZZ$, $gg \to H^* \to ZZ$ and their interference are generated using Sherpav2.2.2 [18] with OpenLoops [19] and the NNPDF3.0 NNLO PDF set. Mass-dependent NLO QCD K-factors are applied, and a further mass-independent K-factor is applied to correct the cross-section to next-to-next-to-next-to leading order (N^3LO) in QCD. $q\bar{q} \to (H^* \to)ZZ + 2j$, the inclusive electroweak (EW) production of ZZ and two jets, is modeled by MadGraph5_aMC@NLO at LO QCD using the NNPDF3.0 NNLO PDF set, and Pythia8.244 is used for parton showering. The leading background $q\bar{q} \to ZZ$ is simulated at NLO in QCD by Sherpav2.2.2 with OpenLoops, using the NNPDF3.0 NNLO PDF set. The WZ, Z+jets, and triboson processes (ZZZ, WZZ, WWZ) are simulated by Sherpav2.2.2 while $t\bar{t} + V$ (V = Wor Z) samples are generated by MadGraph5_aMC@NLO with Pythia8.210 for parton showering.

6 Analysis

The event selection and analysis strategy are the same as that in Ref [1], and are only briefly summarized here.

6.1 $ZZ \to 4\ell$ analysis

In the $ZZ \to 4\ell$ decay channel, where ℓ is μ or e, two on-shell Z bosons are required and the mass of the lepton pairs is compatible with m_Z. Control regions (CR) are defined in the background-enriched 180 GeV $< m_{4l} <$ 220 GeV region, with the signal regions being in the $m_{4l} >$ 220 GeV range. The SRs are defined based on the number of jets to separate ggF and electroweak (EW) Higgs boson production. The jet multiplicity is also introduced in the CRs to better mimic the background in SRs. A deep neural network (NN), implemented using Keras [20] with TensorFlow [21] as the back-end, is trained with the SM samples for Higgs signal (S), interfering background (B) ($gg \to ZZ$) and non-interfering background (NI) ($qq \to ZZ$). The network output is the probability of a given event falling into each of the input categories. The final observable is constructed as follows, with P representing the corresponding probability:

$$O_{\mathrm{NN}} = \log_{10} \frac{P_{\mathrm{S}}}{P_{\mathrm{B}} + P_{\mathrm{NI}}} \tag{11}$$

The NN inputs include matrix elements, the transverse momenta of the two Z bosons, the invariant mass m_{4l}, and other kinematic variables.

Figures 3 and 4 present the cross-section distributions of the observed and expected NN-based observables in each SR, together with respectively the $O_{\varphi G}$linear and quadratic and $O_{t\varphi}$ linear and quadratic fits, presented in Section 8.

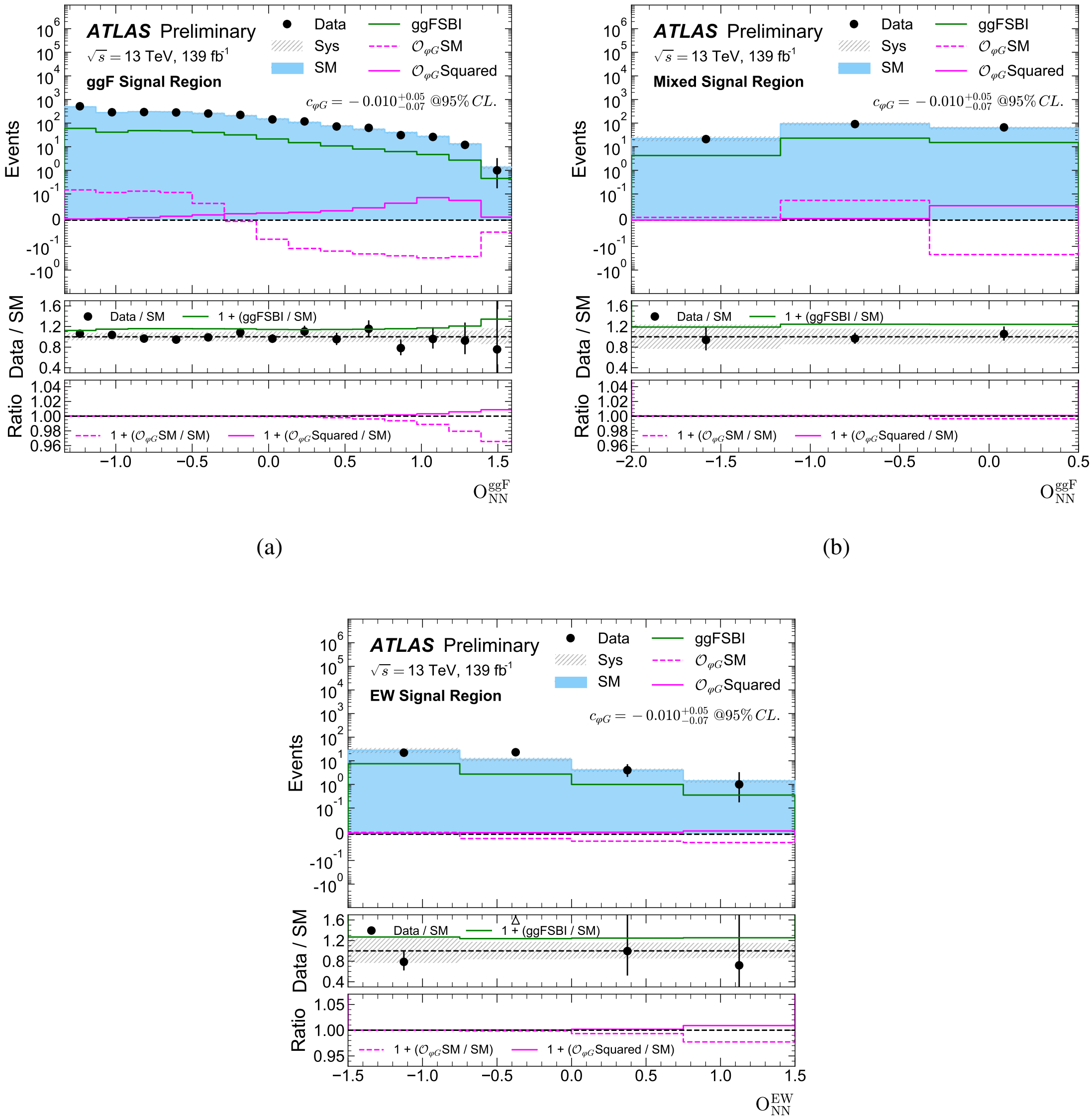

(a)

(b)

(c)

Figure 3: The event cross-section distributions for the 4ℓ channel in 3(a) the ggF SR, 3(b) the mixed SR, and 3(c) the EW SR, as a function of the neural network based observables. Both EFT dimension-six linear ($O_{\varphi G}$SM) and quadratic ($O_{\varphi G}$Squared) contributions are considered in the fit. In the top panel, the dots with error bars are the observed data, while the SM prediction includes the SM $q\bar{q} \to ZZ$ background, the SM $gg \to (H^* \to)ZZ$ (signal plus background plus interference, ggFSBI as shown) process, the SM EW $qq \to (H^* \to)ZZ + 2j$ (signal plus background plus interference) process, and all other SM backgrounds (Z+jets, $t\bar{t}$, triboson and $t\bar{t}V$). The EFT dimension-six linear and quadratic contributions are given with the observed best-fit value from the combined linear and quadratic fit as well as that of SM $gg \to (H^* \to)ZZ$, for comparison. The underflow and overflow are included in the first bin and last bin, respectively. The bottom panels show the ratios to the SM prediction. The total systematic uncertainties described in Section 7 are illustrated by the hatched area.

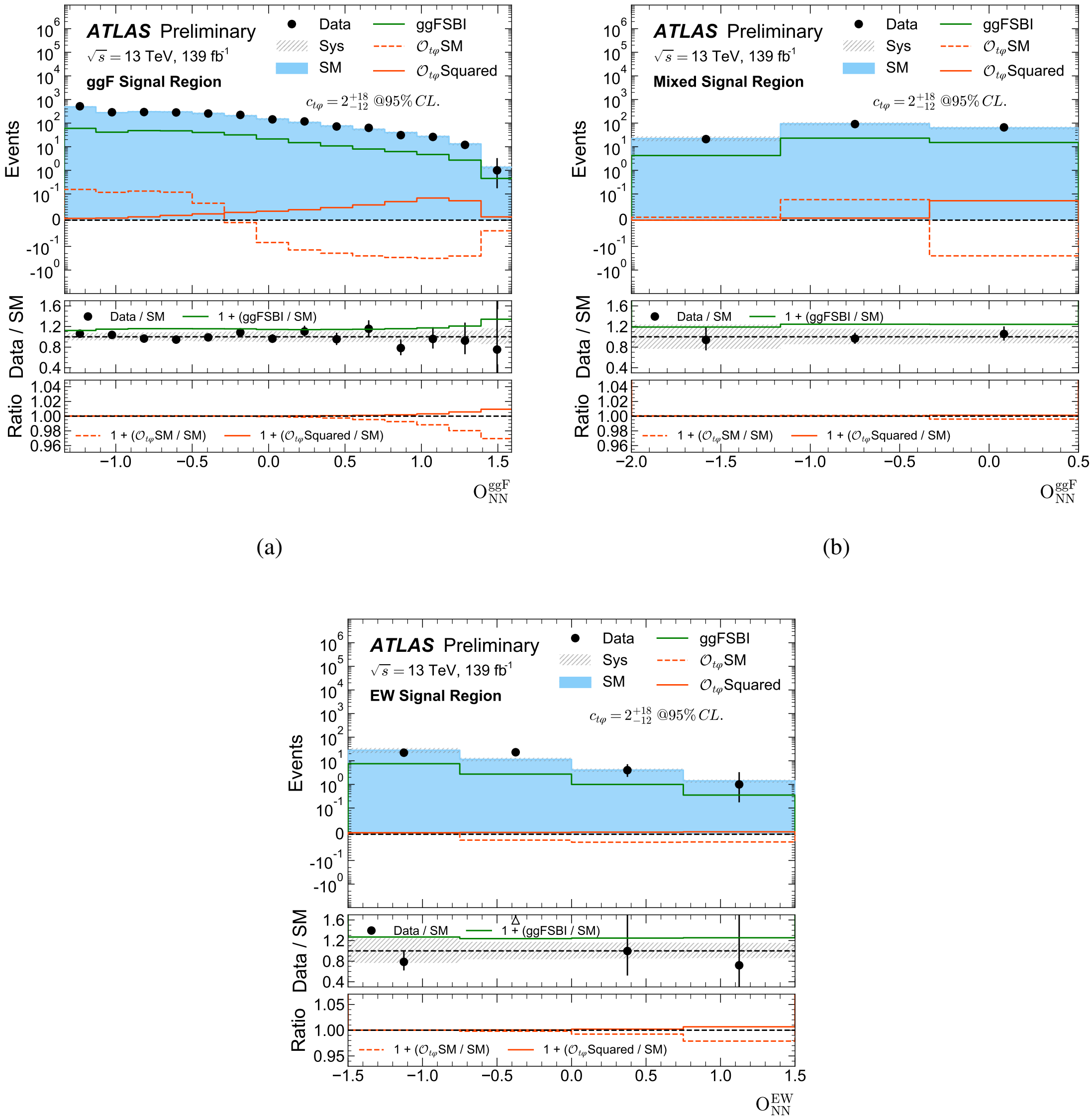

(a)

(b)

(c)

Figure 4: The event cross-section distributions for the 4ℓ channel in 4(a) the ggF SR, 4(b) the mixed SR, 4(c) the EW SR, as a function of the neural network based observables. Both EFT dimension-six linear ($O_{t\varphi}$SM) and quadratic ($O_{t\varphi}$Squared) contributions are considered in the fit. In the top panel, the dots with error bars are the observed data, while the SM prediction includes the SM $q\bar{q} \to ZZ$ background, the SM $gg \to (H^* \to)ZZ$ (signal plus background plus interference, ggFSBI as shown) process, the SM EW $qq \to (H^* \to)ZZ + 2j$ (signal plus background plus interference) process, and all other SM backgrounds (Z+jets, $t\bar{t}$, triboson and $t\bar{t}V$). The EFT dimension-six linear and quadratic contributions are given with the observed best-fit value from the combined linear and quadratic fit as well as that of SM $gg \to (H^* \to)ZZ$, for comparison. The underflow and overflow are included in the first bin and last bin, respectively. The bottom panels show the ratios to SM prediction. The total systematic uncertainties described in Section 7 are illustrated by the hatched area.

6.2 $ZZ \rightarrow 2\ell 2\nu$ analysis

The final state in the $ZZ \rightarrow 2\ell 2\nu$ channel consists of a pair of isolated leptons (e or μ) and large $E_{\mathrm{T}}^{\mathrm{miss}}$ from undetectable neutrinos. Compared with the 4l channel, the branching ratio of the $2\ell 2\nu$ channel is much larger but it suffers a larger background contamination as well. The main backgrounds include $q\bar{q} \rightarrow ZZ$, WZ, non-resonant-$\ell\ell$ (originating from $qq \rightarrow WW$, $t\bar{t}$ and single-top production), and Z + jets. The $q\bar{q} \rightarrow ZZ$ background is estimated from the CRs in the 4ℓ channel while others are extracted from dedicated CRs defined for the $2\ell 2\nu$ channel only. There are three SRs, i.e., ggF SR, mixed SR and EW SR, as in the 4ℓ channel 6.1.

The observable used in the $ZZ \rightarrow 2\ell 2\nu$ analysis is the transverse mass of the two Z bosons,

$$m_{\mathrm{T}}^{ZZ} \equiv \sqrt{\left[\sqrt{m_Z^2 + (p_{\mathrm{T}}^{\ell\ell})^2} + \sqrt{m_Z^2 + (E_{\mathrm{T}}^{\mathrm{miss}})^2}\right]^2 - \left|\vec{p}_{\mathrm{T}}^{\,\ell\ell} + \vec{E}_{\mathrm{T}}^{\mathrm{miss}}\right|^2} \tag{12}$$

where m_Z is the PDG Z boson mass [22], $p_{\mathrm{T}}^{\ell\ell}$ is the transverse momentum of the lepton pair and $E_{\mathrm{T}}^{\mathrm{miss}}$ is the missing transverse energy.

The observed and expected cross-section distributions in each SR are shown in Figures 5 and 6 for the $O_{\varphi G}$ and $O_{t\varphi}$ linear and quadratic fits, respectively, presented in Section 8.

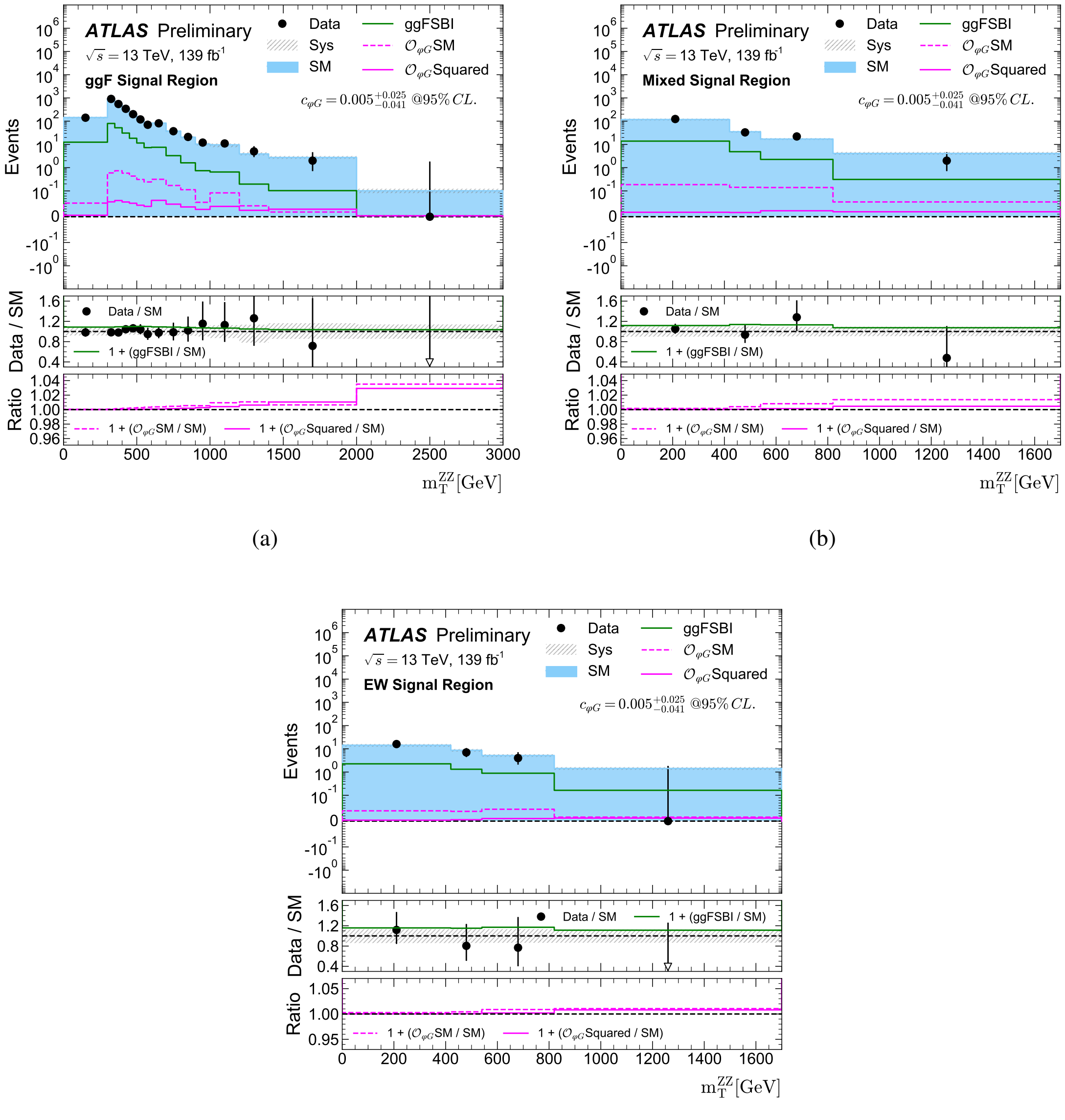

(a)

(b)

(c)

Figure 5: Event cross-section distributions for the $2\ell 2\nu$ channel in 5(a) the ggF SR, 5(b) the mixed SR, 5(c) and the EW SR, plotted as a function of the transverse mass m_{T}^{ZZ}. Both EFT dimension-six linear ($O_{\varphi G}$SM) and quadratic ($O_{\varphi G}$Squared) contributions are considered in the fit. In the top panel, the dots with error bars are the observed data, while the SM prediction includes the dominant background processes SM $q\bar{q} \to ZZ$, SM WZ, SM non-resonant $\ell\ell$, SM $gg \to (H^* \to)ZZ$ (signal plus background plus interference, ggFSBI as shown), SM EW $q\bar{q} \to (H^* \to)ZZ + 2j$ (signal plus background plus interference) and all other SM background (Z+jets, $t\bar{t}$, triboson and $t\bar{t}V$). The EFT dimension-six linear and quadratic contributions are given with the observed best-fit value from the combined linear and quadratic fit as well as that of SM $gg \to (H^* \to)ZZ$, for comparison. The underflow and overflow are included in the first bin and last bin, respectively. The bottom panels show the ratios to the SM prediction. The total systematic uncertainties described in Section 7 are illustrated by the hatched area.

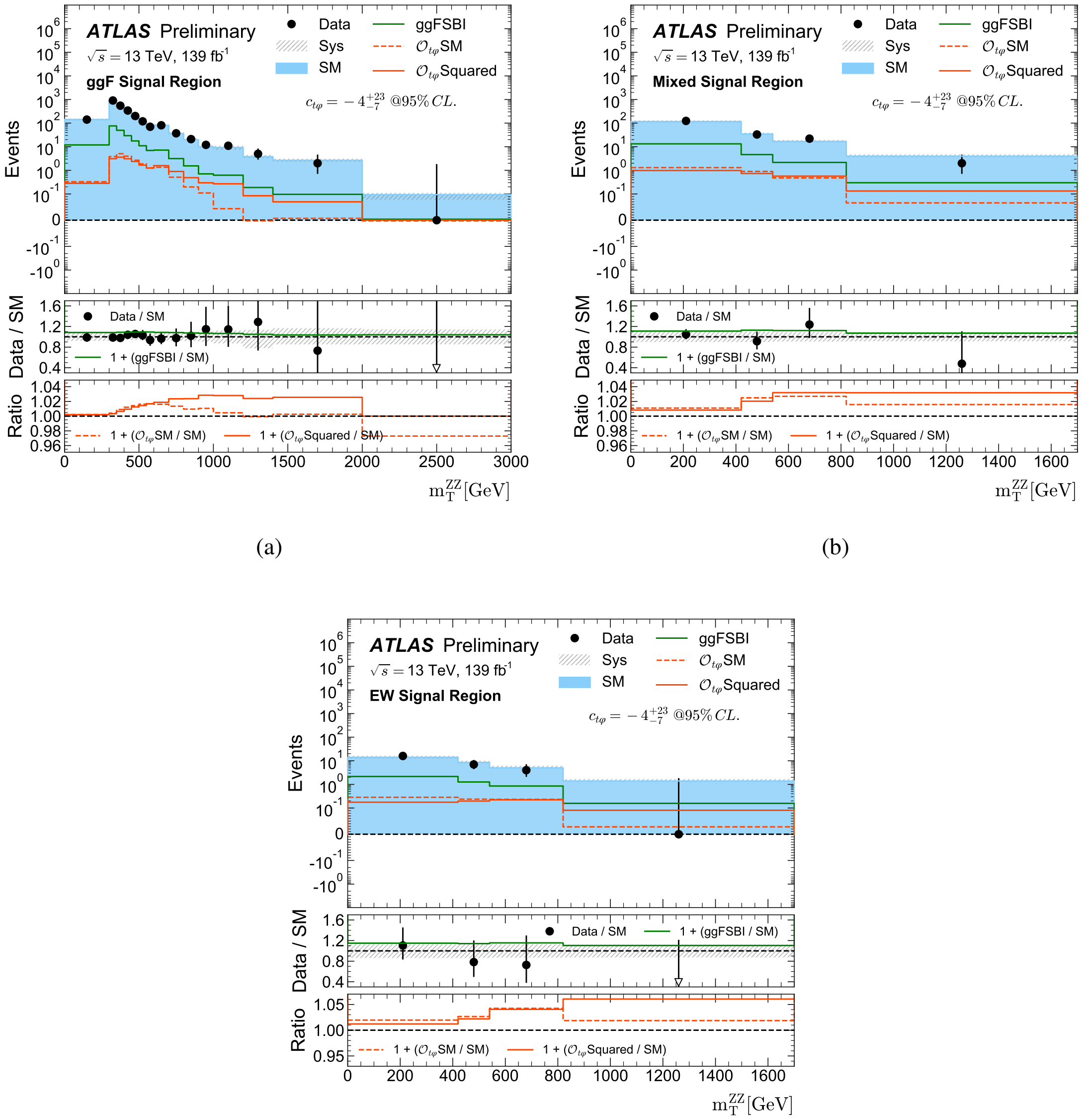

(a)

(b)

(c)

Figure 6: Event cross-section distributions for the $2\ell 2\nu$ channel in 6(a) the ggF SR, 6(b) the mixed SR, 6(c) the EW SR, as a function of the transverse mass m_{T}^{ZZ}. Both EFT dimension-six linear ($O_{t\varphi}$SM) and quadratic ($O_{t\varphi}$Squared) contributions are considered in the fit. In the top panel, the dots with error bars are the observed data, while the SM prediction includes the dominant background processes SM $q\bar{q} \to ZZ$, SM WZ, SM non-resonant $\ell\ell$, SM $gg \to (H^* \to)ZZ$ (signal plus background plus interference, ggFSBI as shown), SM EW $q\bar{q} \to (H^* \to)ZZ + 2j$ (signal plus background plus interference) and all other SM background (Z+jets, $t\bar{t}$, triboson and $t\bar{t}V$). The EFT dimension-six linear and quadratic contributions are given with the observed best-fit value from the combined linear and quadratic fit as well as that of SM $gg \to (H^* \to)ZZ$, for comparison. The underflow and overflow are included in the first bin and last bin, respectively. The bottom panels show the ratios to the SM prediction. The total systematic uncertainties described in Section 7 are illustrated by the hatched area.

7 Systematic uncertainties

The analysis is impacted by systematic uncertainties in the theoretical description of the SM and BSM processes in question, and experimental uncertainties relating to the detector response. All uncertainties applying to SM processes are determined in the same fashion as in Ref. [1], and are discussed only briefly here.

Experimental uncertainties are generally small for both BSM and SM processes except those from jet reconstruction, e.g. jet energy scale and resolution. The systematic uncertainties are dominated by the theoretical modeling of the SM processes, including missing higher-order corrections from perturbative QCD and EW calculations and uncertainties in the modeling of the parton shower.

The following theoretical uncertainties on the BSM processes are taken into account:

Choice of the parton distribution function. Following the procedure adopted for estimating this uncertainty in the SM processes, the PDF uncertainty is evaluated by estimating 100 MC replicas, using the principal component analysis (PCA) [23] method. The uncertainty ranges from 1% to 2%.

Missing higher orders in the strong coupling constant α_S. This type of uncertainty is estimated by varying the renormalization and factorization energy scales up and down by a factor of two from the central value. The uncertainty ranges from 20% to 30%.

Uncertainties due to missing higher-order QCD corrections to the EFT processes (evaluated by varying the EFT renormalization scale, μ_{EFT}) are currently only available for processes such as $t\bar{t}H$ [24] that are tree-level at leading order and hence were not considered in this analysis. Uncertainties due to missing higher-dimensional SMEFT corrections were also not considered due to the unavailability of the necessary theoretical calculations.

8 Results

To probe the impact of EFT operators on Higgs boson couplings in the off-shell region in the $ZZ \rightarrow 4\ell$ and $ZZ \rightarrow 2\ell 2\nu$ decay channels, the profile likelihood technique [25] is employed.

From Equation 9, the expected number of events from the SM and the $O_{\varphi G}$ linear plus quadratic contributions in each bin, referred as ν^{SMEFT}, for a given $c_{\varphi G}$ is:

$$\nu^{\mathrm{SMEFT}}(c_{\varphi G}, \boldsymbol{\theta}) = n^{\mathrm{SM}}_{\mathrm{N^3LO}}(\boldsymbol{\theta}) \times \left(1 + c_{\varphi G} \cdot \frac{n^{O_{\varphi G}\,\mathrm{SM}}_{\mathrm{LO}}(\boldsymbol{\theta})}{n^{\mathrm{SM}}_{\mathrm{LO}}(\boldsymbol{\theta})} + c^2_{\varphi G} \cdot \frac{n^{O_{\varphi G}\,\mathrm{Squared}}_{\mathrm{LO}}(\boldsymbol{\theta})}{n^{\mathrm{SM}}_{\mathrm{LO}}(\boldsymbol{\theta})} \right) \tag{13}$$

where $\boldsymbol{\theta}$ represents nuisance parameters including the effects of systematic and MC statistical uncertainties, constrained using Gaussian and Poisson terms, respectively. n stands for the number of events in each bin. ν^{SMEFT} is parameterized similarly for $c_{t\varphi}$.

A binned likelihood function is then constructed as a product of Poisson probability terms over all bins and fitted to the observed data or the expected SM prediction in all the SRs and CRs simultaneously. The likelihood depends on the parameters of interest, $c_{\varphi G}$ and $c_{t\varphi}$, and a set of nuisance parameters $\boldsymbol{\theta}$.

The observed and expected results based on the profile likelihood ratios (denoted by $-2\ln(\lambda)$) are presented in Figure 7 including linear only and linear plus quadratic fits for each Wilson coefficient (the other is set as 0) of the operators modifying the Higgs-gluon effective coupling or the Higgs-top coupling. The observed (expected) result of $c_{t\varphi}$ in the linear and quadratic fit is -1^{+19}_{-8} (0^{+17}_{-9}) at the 95% confidence level, which is comparable to the result from the boosted $t\bar{t}H$ analysis by CMS [26]. Another study [27] shows that the transverse-momentum differential cross-section analysis in the on-shell Higgs region has a much better resolution in the $c_{t\varphi}$ and $c_{\varphi G}$ than this analysis. The advantage of this analysis is that the high mass region (at the TeV level) has been exploited where new physics may arise. Figure 8 shows 2D contour projections of $-2\ln(\lambda)$ on the Wilson coefficient plane in the asymptotic approximation. The results are consistent with the SM prediction within uncertainties.

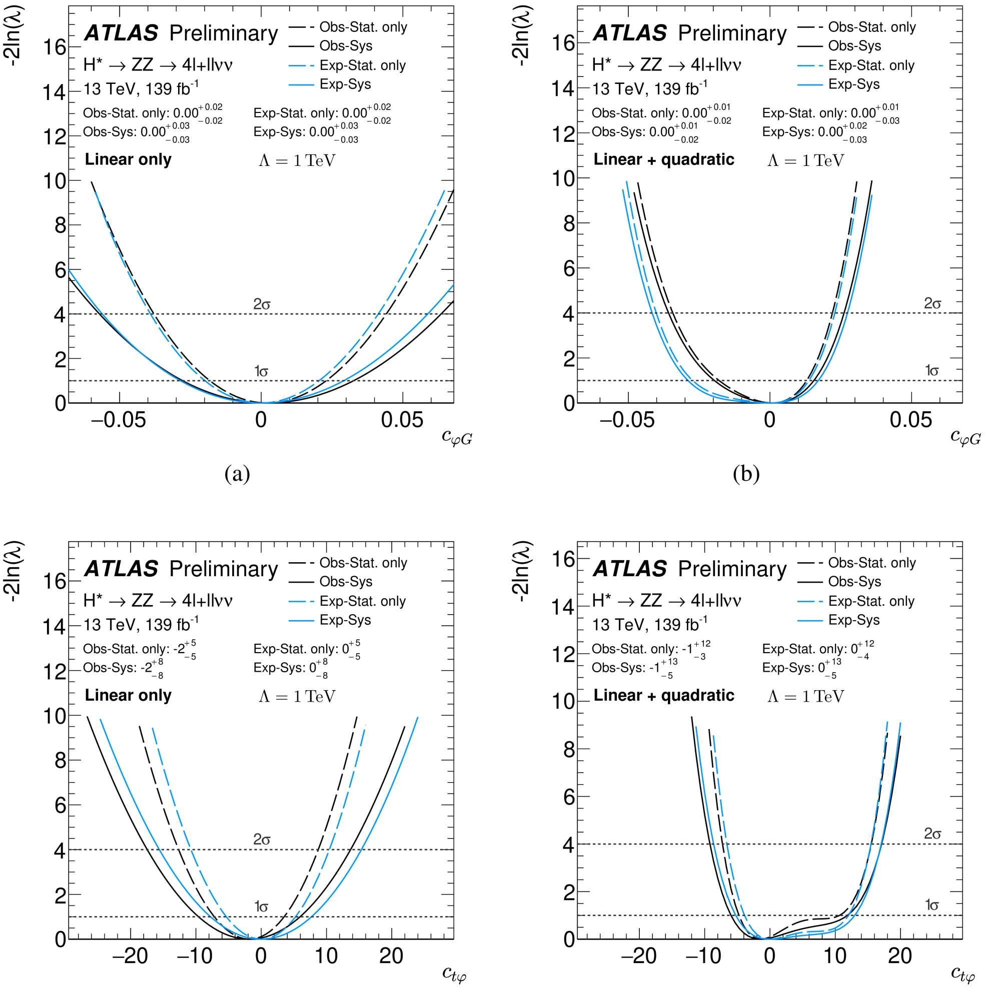

(a)

(b)

(c)

(d)

Figure 7: Negative log-likelihood, $-2\ln(\lambda)$, as a function of dimension-six EFT coefficients 7(a) $c_{\varphi G}$ (Higgs-gluon) with the linear term only, 7(b) $c_{\varphi G}$ with linear and quadratic terms, 7(c) $c_{t\varphi}$ (Higgs-top modifier) with the linear term only, and 7(d) $c_{t\varphi}$ with linear and quadratic terms for the combined analysis of the $ZZ \rightarrow 4\ell$ and $ZZ \rightarrow 2\ell 2\nu$ channels. Only one dimension-six coefficient is fit while the other is set to 0. The dashed curves represent scans with statistical uncertainty only while the scans with full systematic and statistical uncertainties are drawn in the solid curves. The 1 and 2σ confidence levels are calculated using the asymptotic limit.

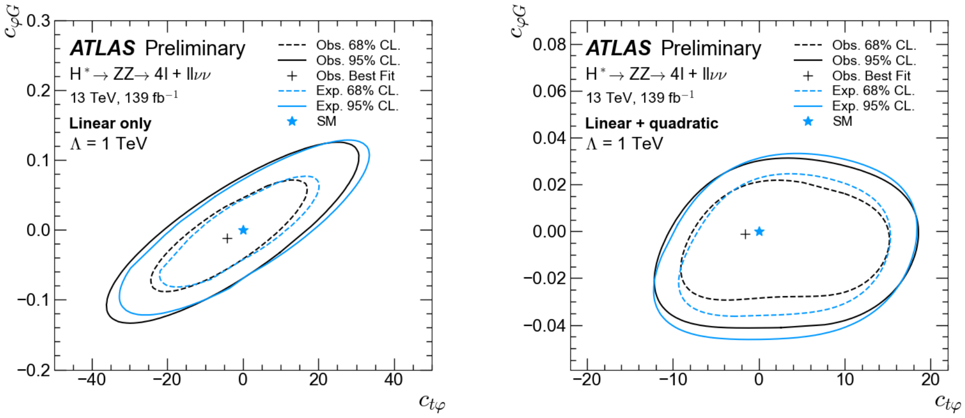

(a) (b)

Figure 8: Projection of negative log-likelihood, $-2\ln(\lambda)$, on the plane of the dimension-six EFT coefficients $c_{\varphi G}$ (Higgs-gluon) and $c_{t\varphi}$ (Higgs-top modifier) for 8(a) linear term only and 8(b) both linear and quadratic terms included, in the combined analysis of the $ZZ \rightarrow 4\ell$ and $ZZ \rightarrow 2\ell 2\nu$ channels. The dashed curves represent scans with statistical uncertainty only while the solid curves include full systematic and statistical uncertainties. The confidence levels are calculated using the asymptotic approximation.

9 Conclusion

Off-shell Higgs boson production with a high invariant mass at the TeV level is potentially sensitive to new physics beyond the Standard Model. Additionally, the degeneracy of the Higgs-top quark and effective Higgs-gluon couplings is broken in the off-shell region, enabling separate measurements of the coupling modifiers.

This note presents the EFT interpretation of off-shell Higgs boson production measured in the $ZZ \rightarrow 4\ell$ and $ZZ \rightarrow 2\ell 2\nu$ decay channels to constrain BSM phenomena. The theoretical frameworks based on the $c_t - c_g$ and the Warsaw basis are demonstrated, as well as how to translate between each other. This measurement is based on the 139 fb^{-1} of proton-proton collision data at the centre-of-mass energy of 13 TeV by the ATLAS experiment at the Large Hadron Collider. The Wilson coefficients associated with the couplings are observed (expected) as -1^{+19}_{-8} (0^{+17}_{-9}) for $c_{t\varphi}$ (Higgs-top coupling modifier) and $0.00^{+0.03}_{-0.04}$$(0.00^{+0.03}_{-0.04})$ for $c_{\varphi G}$ (Higgs-gluon coupling modifier) at the 95% confidence level with dimension-six linear and quadratic contributions included. This note gives the observed event yields in each region for both $ZZ \rightarrow 4\ell$ and $ZZ \rightarrow 2\ell 2\nu$ decay channels and the fitted dimension-six cross-section distributions. The linear-only and two-dimensional scans are also performed. No significant deviation from the SM is observed.

References

[1] ATLAS Collaboration, *Evidence of off-shell Higgs boson production from ZZ leptonic decay channels and constraints on its total width with the ATLAS detector*, (2023), arXiv: 2304.01532 [hep-ex] (cit. on pp. 2, 6–8, 14).

[2] N. Kauer and G. Passarino, *Inadequacy of zero-width approximation for a light Higgs boson signal*, JHEP **08** (2012) 116, arXiv: 1206.4803 [hep-ph] (cit. on p. 2).

[3] A. Azatov and A. Paul, *Probing Higgs couplings with high p_T Higgs production*, JHEP **2014** (2014) 14, arXiv: 1309.5273 [hep-ph] (cit. on p. 2).

[4] A. Azatov, C. Grojean, A. Paul and E. Salvioni, *Taming the off-shell Higgs boson*, J. Exp. Theor. Phys. **120** (2015) 354, arXiv: 1406.6338 [hep-ph] (cit. on p. 2).

[5] R. M. Abraham, D. Gonçalves, T. Han, S. C. I. Leung and H. Qin, *Directly Probing the Higgs-top Coupling at High Scales*, Physics Letters B **825** (2022) 136839, arXiv: 2106.00018 [hep-ph] (cit. on p. 2).

[6] C. Grojean, E. Salvioni, M. Schlaffer and A. Weiler, *Very boosted Higgs in gluon fusion*, JHEP **120** (2015) 22, arXiv: 1312.3317 [hep-ph] (cit. on pp. 2, 3).

[7] B. Grzadkowski, M. Iskrzynski, M. Misiak and J. Rosiek, *Dimension-Six Terms in the Standard Model Lagrangian*, JHEP **2010** (2010) 85, arXiv: 1008.4884 [hep-ph] (cit. on p. 2).

[8] C. Degrande, G. Durieux, E. V. Fabio Maltoni Ken Mimasu and C. Zhang, *Automated one-loop computations in the standard model effective field theory*, Phys.Rev.D **103** (2021) 096024, arXiv: 2008.11743 [hep-ph] (cit. on pp. 4, 7).

[9] F. Caola and K. Melnikov, *Constraining the Higgs boson width with ZZ production at the LHC*, Phys.Rev.D **88** (2013) 054024, arXiv: 1307.4935 [hep-ph] (cit. on p. 6).

[10] ATLAS Collaboration, *The ATLAS Experiment at the CERN Large Hadron Collider*, JINST **3** (2008) S08003 (cit. on p. 6).

[11] ATLAS Collaboration, *The ATLAS Collaboration Software and Firmware*, ATL-SOFT-PUB-2021-001, 2021, URL: https://cds.cern.ch/record/2767187 (cit. on p. 6).

[12] J. Alwall et al., *The automated computation of tree-level and next-to-leading order differential cross sections, and their matching to parton shower simulations*, JHEP **07** (2014) 079, arXiv: 1405.0301 [hep-ph] (cit. on p. 7).

[13] R. D. Ball et al., *Parton distributions for the LHC run II*, JHEP **04** (2015) 040, arXiv: 1410.8849 [hep-ph] (cit. on p. 7).

[14] O. Mattelaer, *On the maximal use of Monte Carlo samples: re-weighting events at NLO accuracy*, Eur. Phys. J. C **76** (2016) 674, arXiv: 1607.00763 [hep-ph] (cit. on p. 7).

[15] T. Sjöstrand, S. Mrenna and P. Skands, *A brief introduction to PYTHIA 8.1*, Comput. Phys. Commun. **178** (2008) 852, arXiv: 0710.3820 [hep-ph] (cit. on p. 7).

[16] ATLAS Collaboration, *ATLAS Pythia 8 tunes to* 7 *TeV data*, ATL-PHYS-PUB-2014-021, 2014, URL: https://cds.cern.ch/record/1966419 (cit. on p. 7).

[17] M. L. Mangano, M. Moretti, F. Piccinini and M. Treccani, *Matching matrix elements and shower evolution for top-quark production in hadronic collisions*, (2006), arXiv: hep-ph/0611129 [hep-ph] (cit. on p. 7).

[18] E. Bothmann et al., *Event generation with Sherpa 2.2*, SciPost Phys. **7** (2019) 034, arXiv: `1905.09127 [hep-ph]` (cit. on p. 7).

[19] F. Buccioni et al., *OpenLoops 2*, Eur. Phys. J. C **79** (2019) 866, arXiv: `1907.13071 [hep-ph]` (cit. on p. 7).

[20] F. Chollet et al., *Keras*, 2015, URL: `https://keras.io` (cit. on p. 8).

[21] Martín Abadi et al., *TensorFlow: Large-Scale Machine Learning on Heterogeneous Systems*, Software available from tensorflow.org, 2015, URL: `https://www.tensorflow.org/` (cit. on p. 8).

[22] Particle Data Group, P. Zyla et al., *Review of Particle Physics*, PTEP **2020** (2020) 083C01 (cit. on p. 11).

[23] S. Carrazza, S. Forte, Z. Kassabov, J. I. Latorre and J. Rojo, *An Unbiased Hessian Representation for Monte Carlo PDFs*, Eur. Phys. J. C **75** (2015) 369, arXiv: `1505.06736 [hep-ph]` (cit. on p. 14).

[24] F. Maltoni, E. Vryonidou and C. Zhang, *Higgs production in association with a top-antitop pair in the Standard Model Effective Field Theory at NLO in QCD*, JHEP **10** (2016) 123, arXiv: `1607.05330 [hep-ph]` (cit. on p. 14).

[25] G. Cowan, K. Cranmer, E. Gross and O. Vitells, *Asymptotic formulae for likelihood-based tests of new physics*, Eur. Phys. J. C **71** (2011) 1554, arXiv: `1007.1727 [physics.data-an]` (cit. on p. 14), Erratum: Eur. Phys. J. C **73** (2013) 2501.

[26] CMS Collaboration, *Search for new physics using effective field theory in* 13 *TeV* pp *collision events that contain a top quark pair and a boosted Z or Higgs boson*, (2022), arXiv: `2208.12837 [hep-ex]` (cit. on p. 15).

[27] M. Grazzini, A. Ilnicka, M. Spira and M. Wiesemann, *Modeling BSM effects on the Higgs transverse-momentum spectrum in an EFT approach*, Journal of High Energy Physics **2017** (2017), URL: `https://link.springer.com/article/10.1007/JHEP03(2017)115` (cit. on p. 15).

Appendices

A Cross-section distributions in the inclusive region

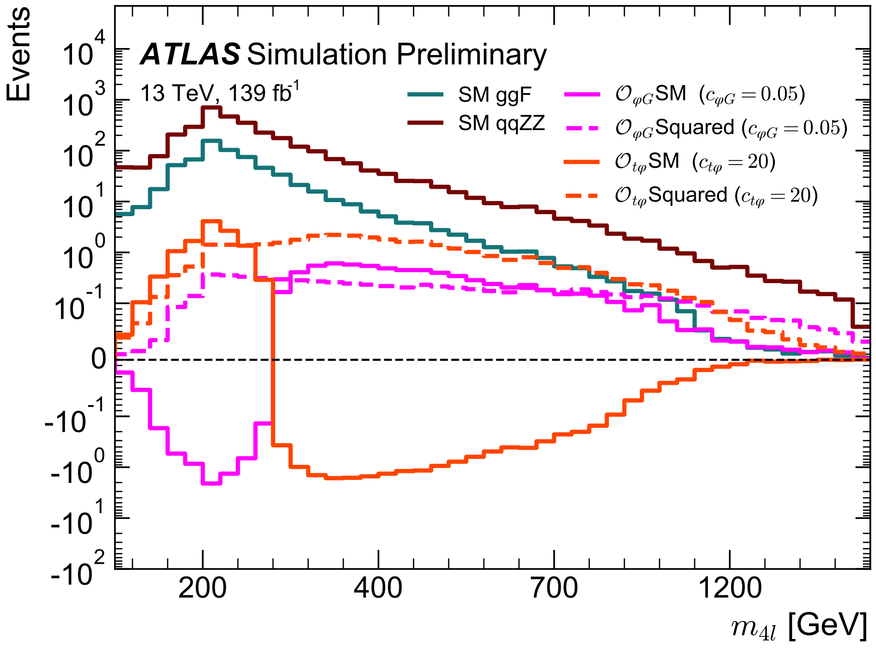

Figure 9: Cross-section distributions of the EFT dimension-six operators in the 4ℓ decay channel, plotted as a function of $m_{4\ell}$, including the $O_{\varphi G}$ linear term ($O_{\varphi G}$SM), the $O_{\varphi G}$ quadratic term ($O_{\varphi G}$Squared), the $O_{t\varphi}$ linear term ($O_{t\varphi}$SM), and the $O_{t\varphi}$ quadratic term ($O_{t\varphi}$Squared). Also shown for comparison are two SM processes, $qq \to ZZ$ production and the total $gg \to ZZ$ SBI. The EFT dimension-six coefficients are set to their own upper 95% limit.

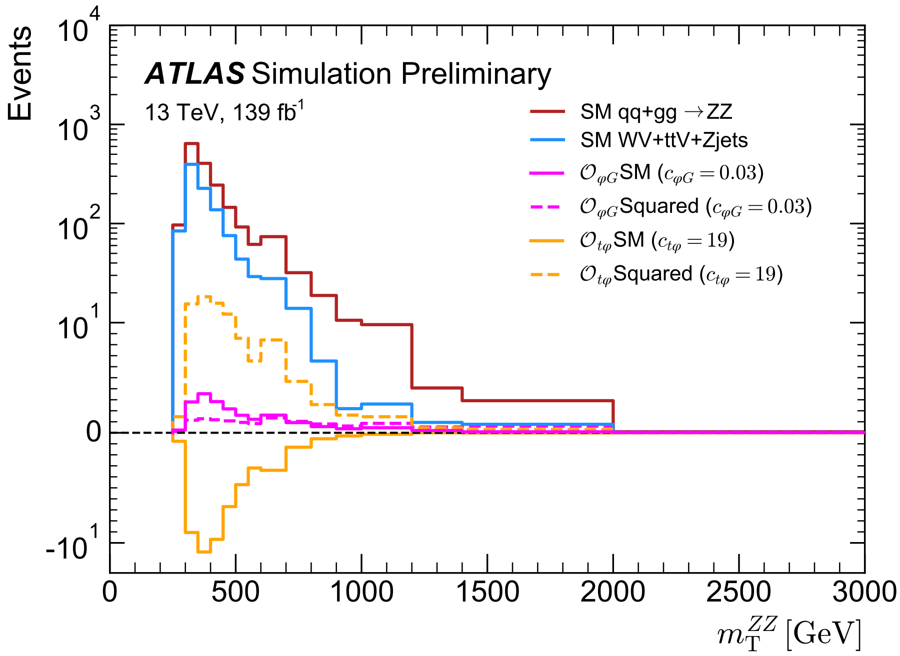

Figure 10: Cross-section distributions of the EFT dimension-six operators in the $2\ell 2\nu$ decay channel, plotted vs. m_{T}^{ZZ}, including the $O_{\varphi G}$ linear term ($O_{\varphi G}$SM), the $O_{\varphi G}$ quadratic term ($O_{\varphi G}$Squared), the $O_{t\varphi}$ linear term ($O_{t\varphi}$SM) and the $O_{t\varphi}$ quadratic term ($O_{t\varphi}$Squared). SM processes are shown for comparison, the combined $qq + gg \rightarrow ZZ$ and other relevant processes. The EFT dimension-six coefficients are set to their own upper 95% limit.

B Cross-section distributions in the linear-only fit

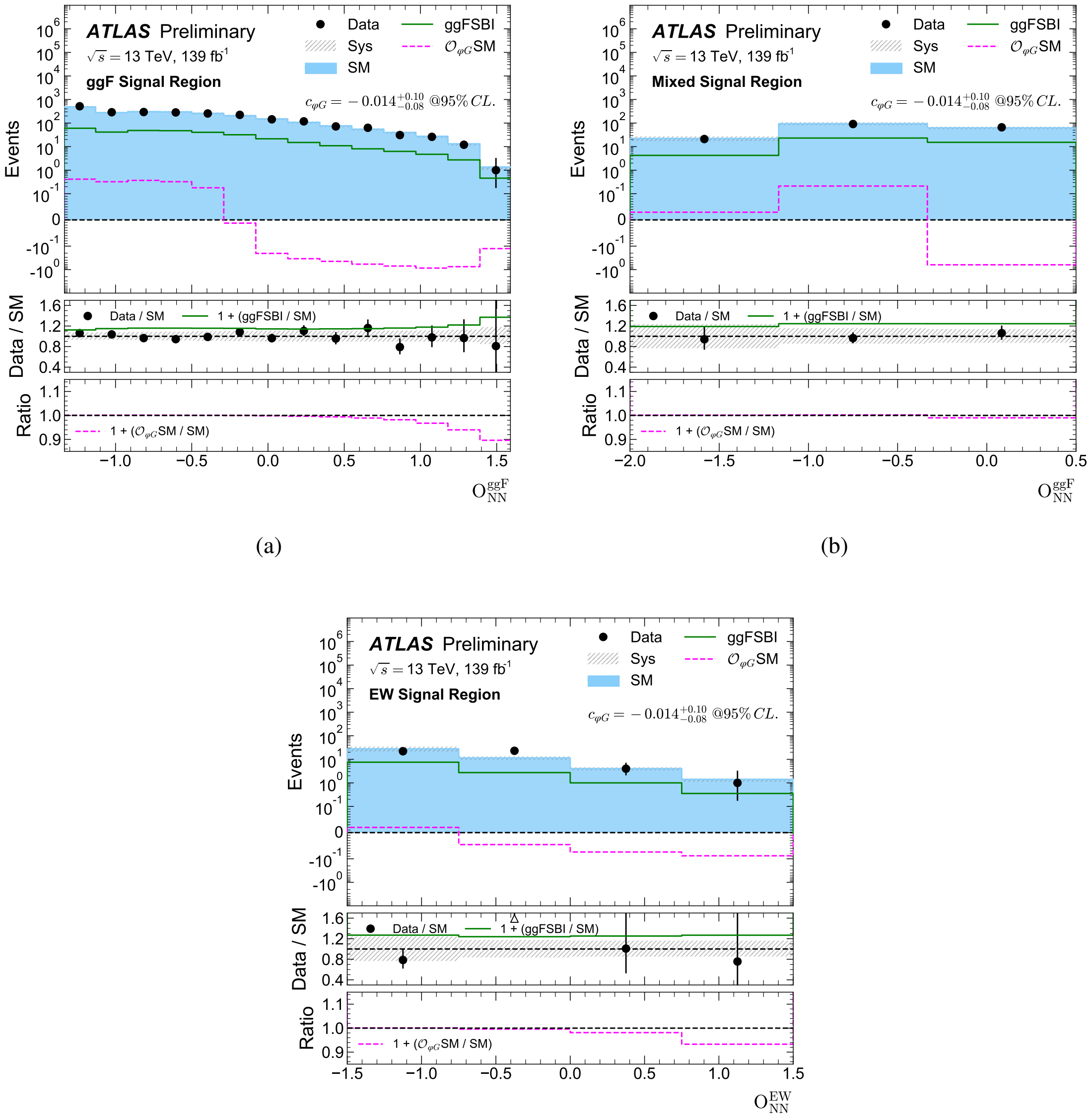

(a) (b) (c)

Figure 11: Event cross-section distributions for the 4ℓ channel in 11(a) the ggF SR, 11(b) the mixed SR, and 11(c) the EW SR, plotted against the neural network based observables. Only the dimension-six linear contribution $O_{\varphi G}$SM is considered in the fit. In the top panel, the black dots with error bars are the observed data, while the blue area represents the SM prediction including the dominant background $qq \to ZZ$, the $gg \to (H^* \to)ZZ$ process (signal plus background plus interference), and the EW $qq \to (H^* \to)ZZ + 2j$ process (signal plus background plus interference), as well as the minor backgrounds (Z+jets, $t\bar{t}$, triboson and $t\bar{t}V$). The EFT dimension-six linear contribution is given with the observed best-fit value from the linear fit as well as that of SM $gg \to (H^* \to)ZZ$, for comparison. The underflow and overflow are included in the first and last bin, respectively. The bottom panels show the ratios to SM prediction. The total systematic uncertainties described in Section 7 are illustrated by the hatched area.

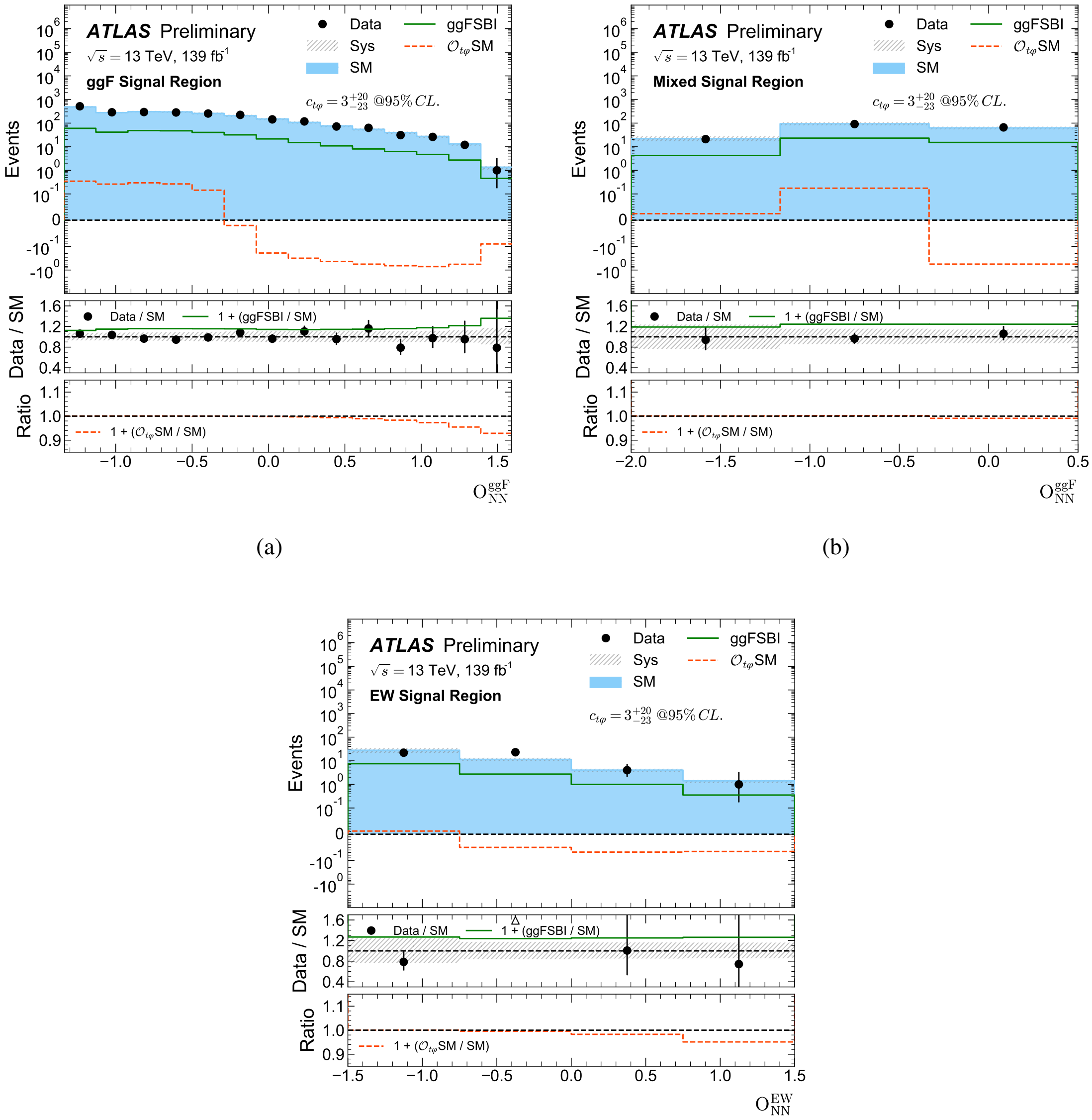

(a)

(b)

(c)

Figure 12: Event cross-section distributions for the 4ℓ channel in 12(a) the ggF SR, 12(b) the mixed SR, and 12(c) the EW SR, plotted against the neural network based observables. Only the dimension-six linear contribution $O_{t\varphi}$SM is considered in the fit. In the top panel, the black dots with error bars are the observed data, while the blue area represents the SM prediction including the dominant background $qq \to ZZ$, the $gg \to (H^* \to)ZZ$ process (signal plus background plus interference), and the EW $qq \to (H^* \to)ZZ + 2j$ process (signal plus background plus interference), as well as the minor backgrounds (Z+jets, $t\bar{t}$, triboson and $t\bar{t}V$). The EFT dimension-six linear contribution is given with the observed best-fit value from the linear fit as well as that of SM $gg \to (H^* \to)ZZ$, for comparison. The underflow and overflow are included in the first and last bin, respectively. The bottom panels show the ratios to the SM prediction. The total systematic uncertainties described in Section 7 are illustrated by the hatched area.

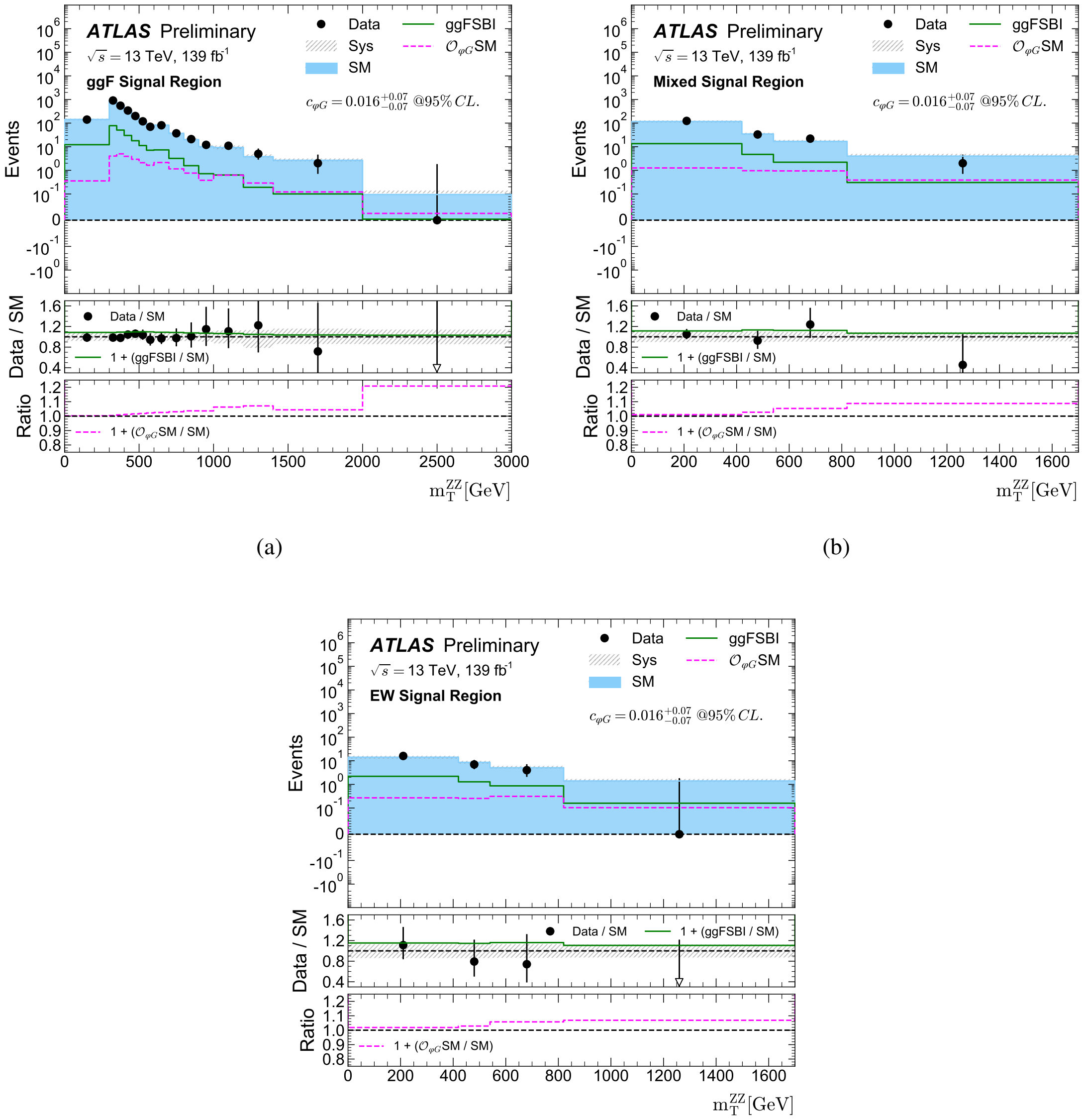

(a)

(b)

(c)

Figure 13: Event cross-section distributions for the $2\ell 2\nu$ channel in 13(a) the ggF SR, 13(b) the mixed SR, and 13(c) the EW SR, plotted against the transverse mass m_T^{ZZ}. Only the dimension-six linear contribution $O_{\varphi G}$SM is considered in the fit. In the top panel, the black dots with error bars are the observed data, while the blue area represents the SM prediction including the dominant background $qq \to ZZ$, the WZ, non-resonant $\ell\ell$, and Z+jets backgrounds, the $gg \to (H^* \to)ZZ$ process (signal plus background plus interference), the EW $qq \to (H^* \to)ZZ + 2j$ process (signal plus background plus interference) and the minor backgrounds (triboson and $t\bar{t}V$). The EFT dimension-six linear contribution is given with the observed best-fit value from the linear fit as well as that of SM $gg \to (H^* \to)ZZ$, for comparison. The underflow and overflow are included in the first and last bin, respectively. The bottom panels show the ratios to the SM prediction. The total systematic uncertainties described in Section 7 are illustrated by the hatched area.

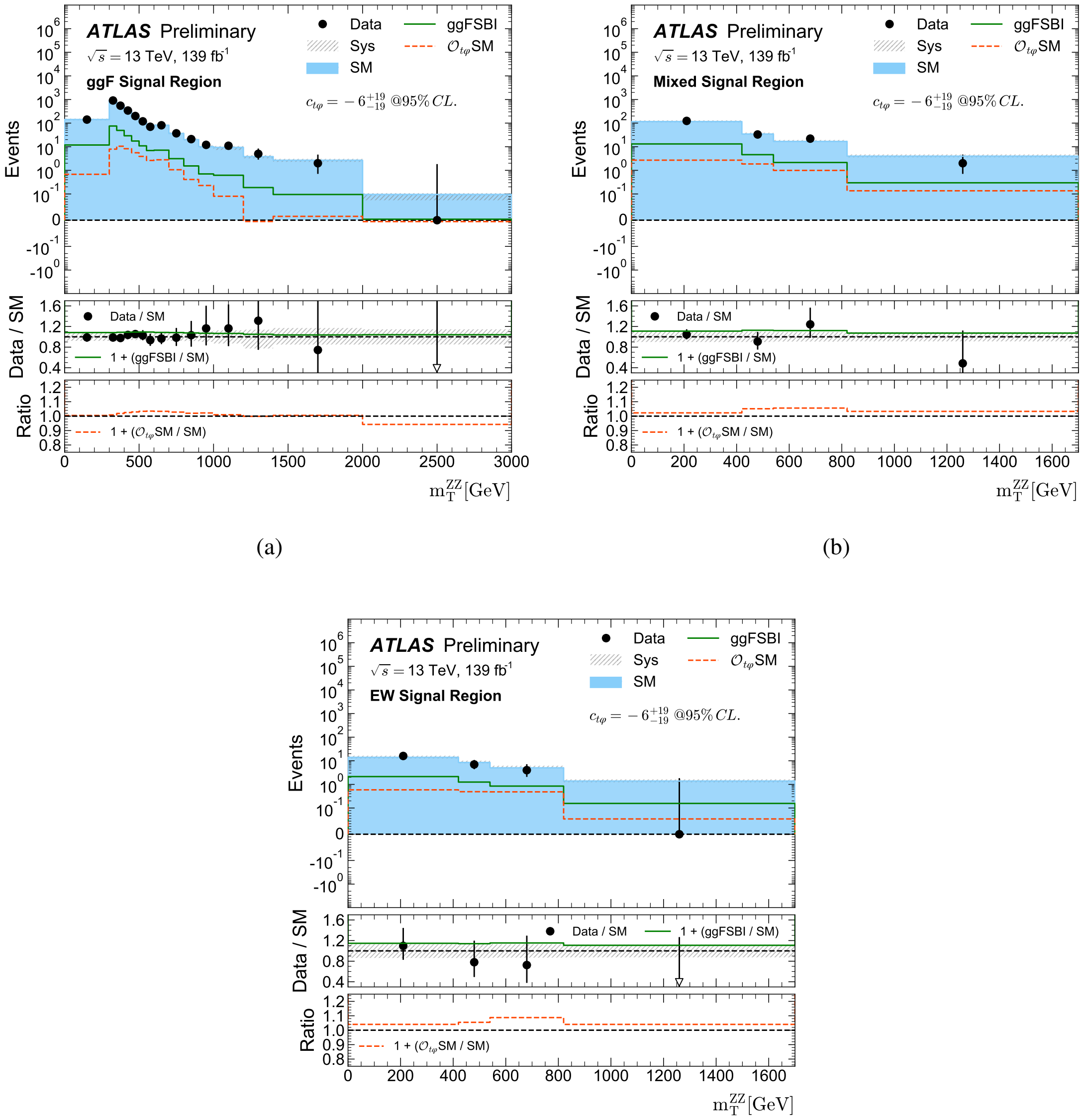

(a)

(b)

(c)

Figure 14: Event cross-section distributions for the $2\ell 2\nu$ channel in 14(a) the ggF SR, 14(b) the mixed SR, 14(c) and the EW SR, plotted against the transverse mass m_T^{ZZ}. Only the dimension-six linear contribution $O_{t\varphi}$SM is considered in the fit. In the top panel, the black dots with error bars are the observed data, while the blue area represents the SM prediction including the dominant background $qq \to ZZ$, the WZ, non-resonant $\ell\ell$, and Z+jets backgrounds, the $gg \to (H^* \to)ZZ$ process (signal plus background plus interference), the EW $qq \to (H^* \to)ZZ + 2j$ process (signal plus background plus interference) and the minor backgrounds (triboson and $t\bar{t}V$). The EFT dimension-six linear contribution is given with the observed best-fit value from the linear fit as well as that of SM $gg \to (H^* \to)ZZ$, for comparison. The underflow and overflow are included in the first and last bin, respectively. The bottom panels show the ratios to the SM prediction. The total systematic uncertainties described in Section 7 are illustrated by the hatched area.

C Results in the individual $ZZ \to 4\ell$ channel

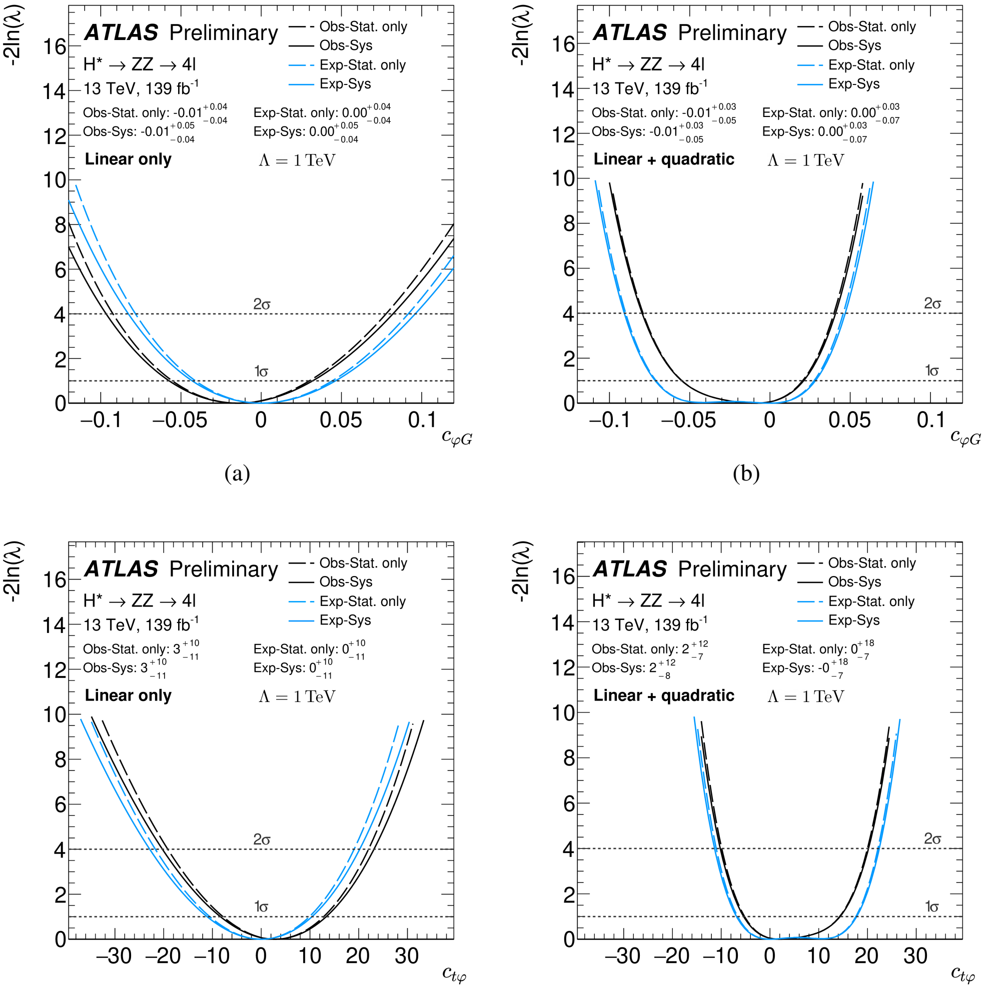

(a)

(b)

(c)

(d)

Figure 15: Negative log-likelihood, $-2\ln(\lambda)$, as a function of dimension-six EFT coefficients 15(a) $c_{\varphi G}$ (Higgs-gluon) with linear term only, 15(b) $c_{\varphi G}$ with linear and quadratic terms, 15(c) $c_{t\varphi}$ (Higgs-top modifier) with linear term only, and 15(d) $c_{t\varphi}$ with linear and quadratic terms for the analysis of the $ZZ \to 4\ell$ channel. The dashed curves represent scans with statistical uncertainty only while the scans with full systematic and statistical uncertainties are drawn in the solid curves. The 1 and 2σ confidence levels are calculated using the asymptotic limit.

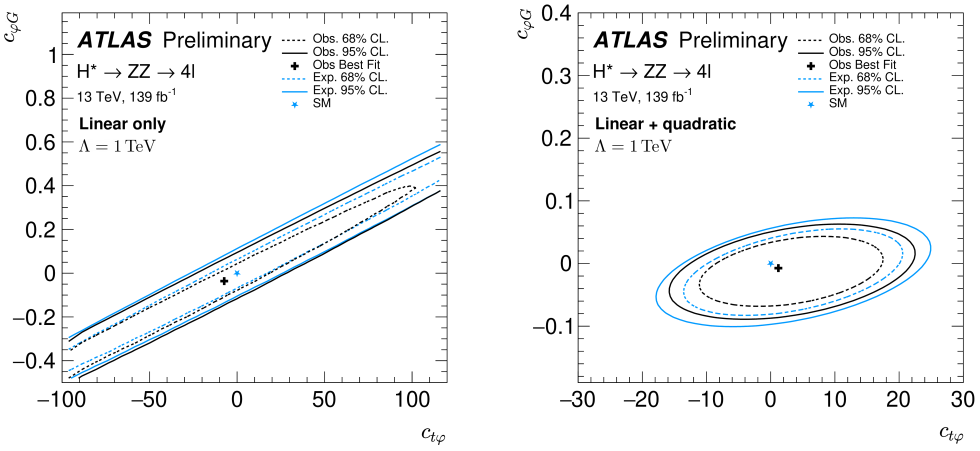

(a)

(b)

Figure 16: Projection of negative log-likelihood, $-2\ln(\lambda)$, on the plane of the dimension-six EFT coefficients $c_{\varphi G}$ (Higgs-gluon) and $c_{t\varphi}$ (Higgs-top modifier) for 16(a) linear term only and 16(b) both linear and quadratic terms included, in the analysis of the $ZZ \to 4\ell$ channel. The boundaries of Figure 16(a) axes are restricted to the EFT validity region: for $c_{\varphi G} < -0.5$ the fitted total yield would be negative, thus invalidating the interpretation. The dashed curves represent scans with statistical uncertainty only while the solid curves include full systematic and statistical uncertainties. The confidence levels are calculated using the asymptotic approximation.

D Results in the individual $ZZ \to 2\ell 2\nu$ channel

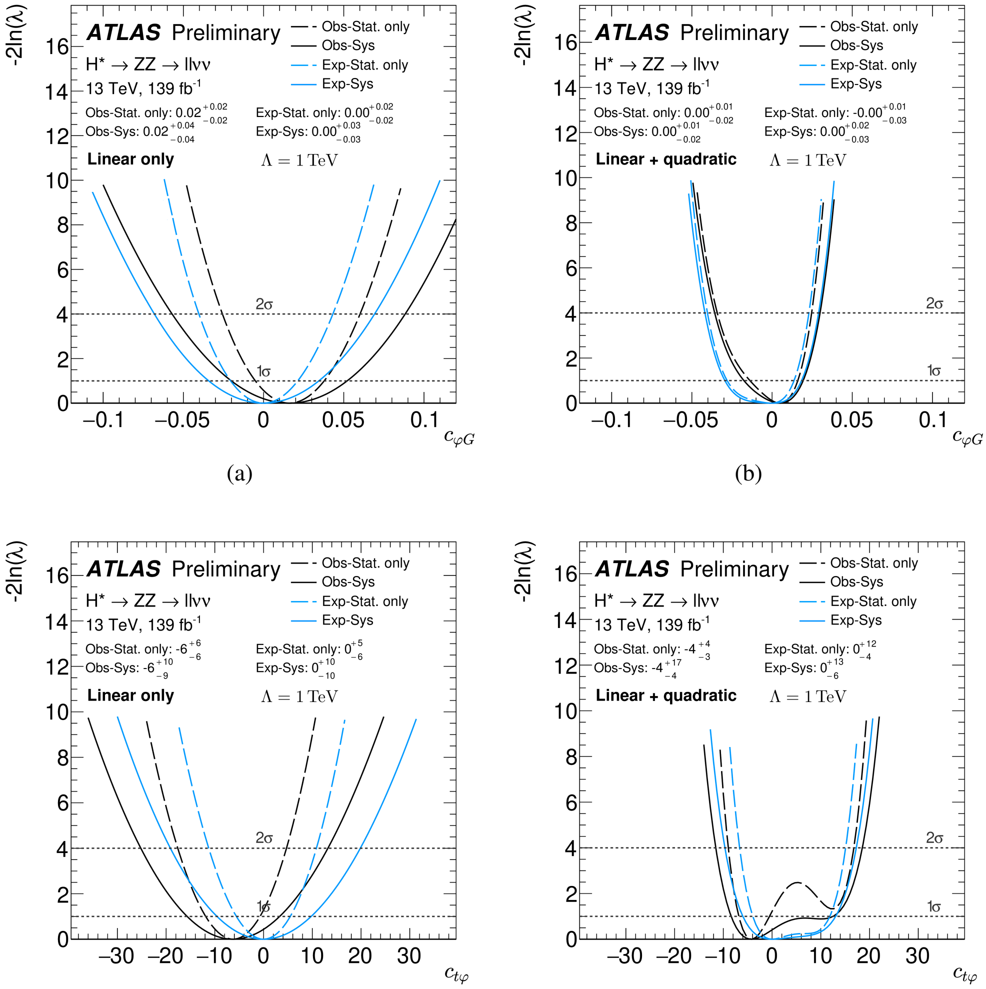

(a)

(b)

(c)

(d)

Figure 17: Negative log-likelihood, $-2\ln(\lambda)$, as a function of dimension-six EFT coefficients 17(a) $c_{\varphi G}$ (Higgs-gluon) with linear term only, 17(b) $c_{\varphi G}$ with linear and quadratic terms, 17(c) $c_{t\varphi}$ (Higgs-top modifier) with linear term only, and 17(d) $c_{t\varphi}$ with linear and quadratic terms for the analysis of the $ZZ \to 2\ell 2\nu$ channel. The dashed curves represent scans with statistical uncertainty only while the scans with full systematic and statistical uncertainties are drawn in the solid curves. The 1 and 2σ confidence levels are calculated using the asymptotic limit.

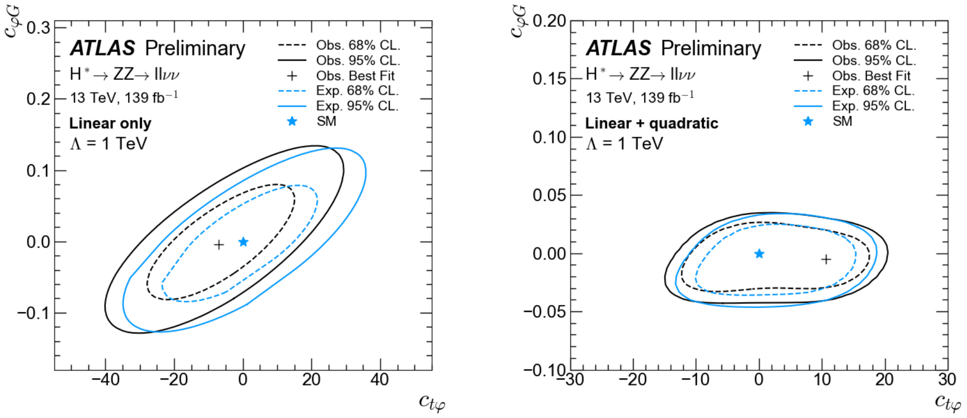

(a)

(b)

Figure 18: Projection of negative log-likelihood, $-2\ln(\lambda)$, on the plane of the dimension-six EFT coefficients $c_{\varphi G}$ (Higgs-gluon) and $c_{t\varphi}$ (Higgs-top modifier) for 18(a) linear term only and 18(b) both linear and quadratic terms included, in the analysis of the $ZZ \longrightarrow 2\ell 2\nu$ channel. The dashed curves represent scans with statistical uncertainty only while the solid curves include full systematic and statistical uncertainties. The confidence levels are calculated using the asymptotic approximation.

E Event display

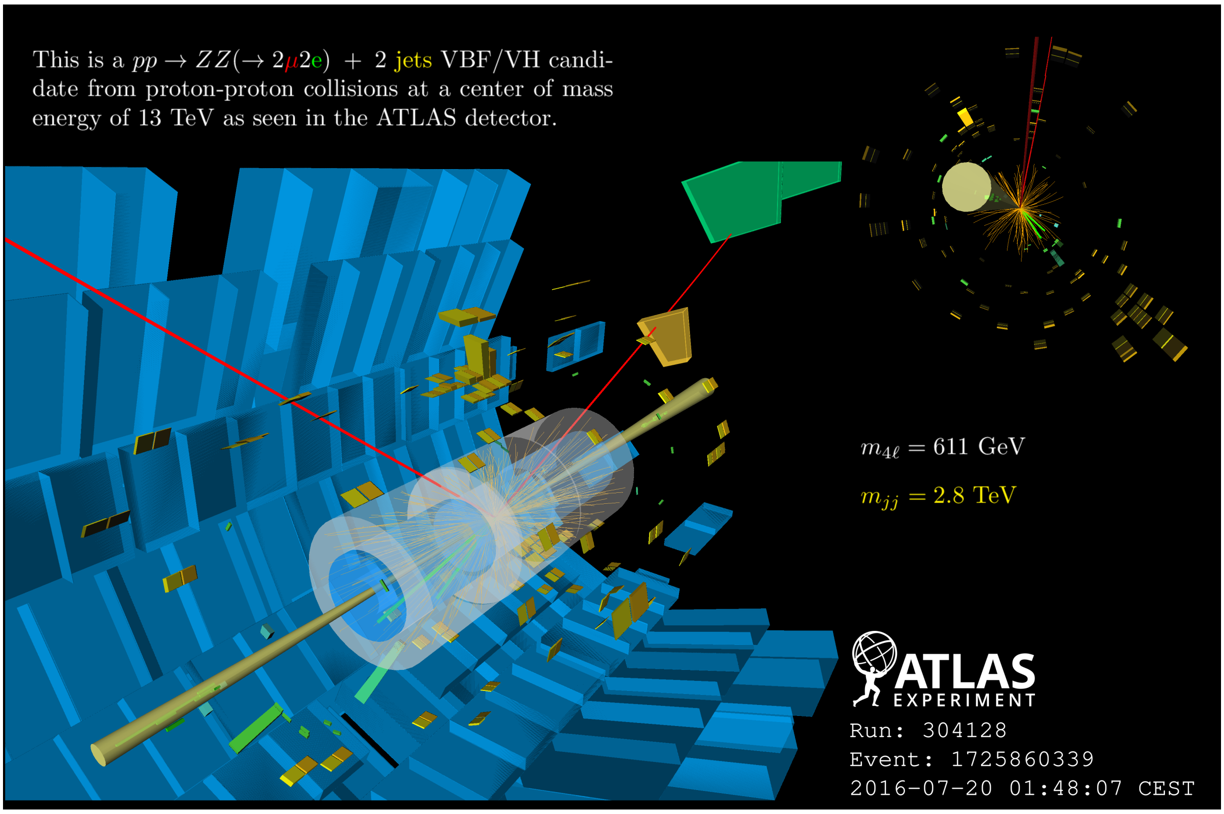

Figure 19: A $pp \to ZZ(\to 2\mu 2e) + 2$ jets VBF/VH candidate from proton-proton collisions at a center of mass energy of 13 TeV as seen in the ATLAS detector, with $m_{4\ell} = 611$ GeV and $m_{jj} = 2.8$ TeV. The red lines indicate muons and the green curves represent electrons. Two forward energetic jets are shown in yellow cones.

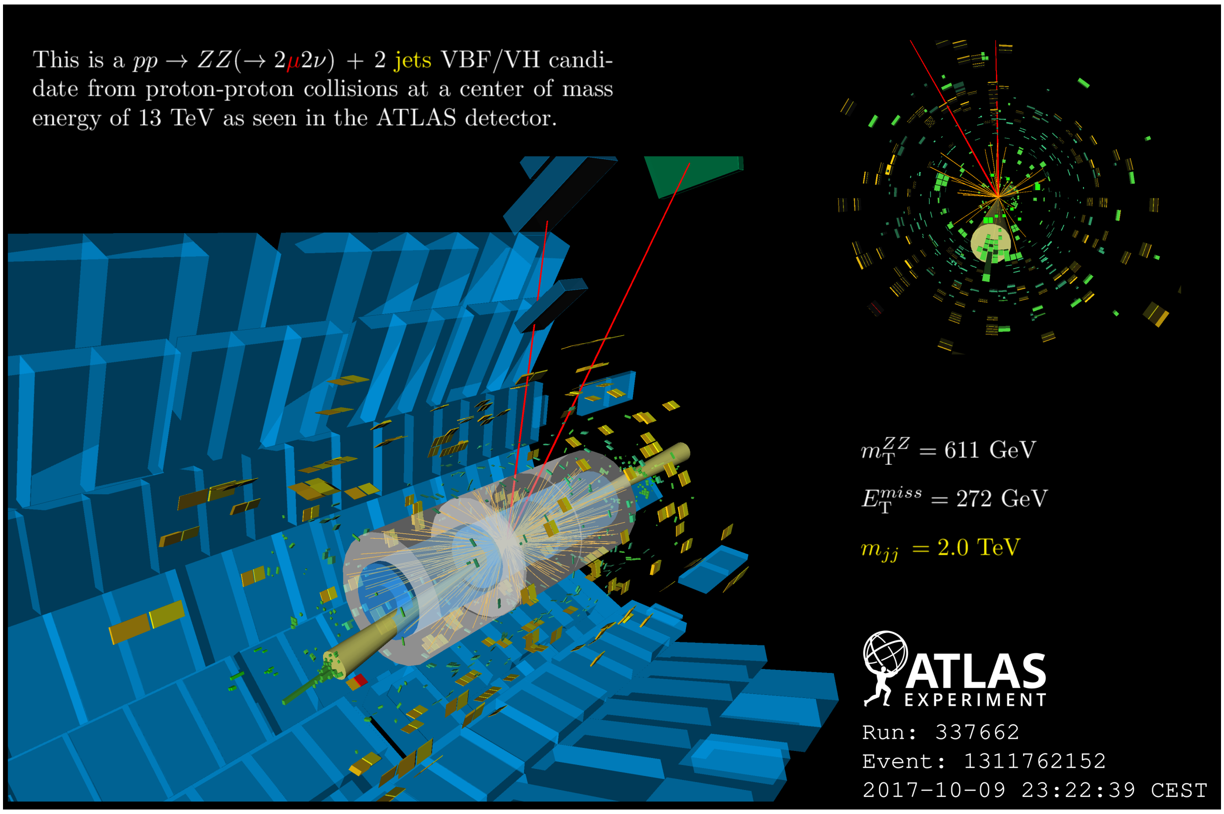

Figure 20: A $pp \to ZZ(\to 2\mu 2\nu)$ + 2 jets VBF/VH candidate from proton-proton collisions at a center of mass energy of 13 TeV as seen in the ATLAS detector, with $m_{\mathrm{T}}^{ZZ} = 611$ GeV, $E_{\mathrm{T}}^{miss} = 272$ GeV and $m_{jj} = 2.0$ TeV. The red lines indicate muons. Two forward energetic jets are shown in yellow cones.